Atmos. Meas. Tech. Discuss., 3, 4761–4789, 2010
www.atmos-meas-tech-discuss.net/3/4761/2010/
doi:10.5194/amtd-3-4761-2010

Atmospheric Measurement Techniques Discussions

Pore structure 3-D imaging by synchrotron micro-tomography of graupel grains

F. Enzmann[1], M. M. Miedaner[1], M. Kersten[1], N. von Blohn[1], S. K. Mitra[1], S. Borrmann[1], M. Stampanoni[2], M. Ammann[2], and T. Huthwelker[2]

[1]Earth System Science Research Centre, Johannes Gutenberg-University, Mainz, Germany
[2]Paul Scherrer Institute, Villigen-PSI, Switzerland

Received: 2 September 2010 – Accepted: 22 September 2010 – Published: 5 November 2010

Correspondence to: M. Kersten (kersten@uni-mainz.de)

Published by Copernicus Publications on behalf of the European Geosciences Union.

Abstract

Three dimensional air bubble structure including size distribution, concentration and spatial distribution are important clues in identifying the growth regime of graupel and hailstone. For imaging of the bubble structure, a cryo-stage was developed to adapt to the standard setup of the SLS X04SA tomography beamline (actually replaced by the TOMCAT beamline) at the Swiss Light Source synchrotron facility to the requirements of ice particle micro-tomography. The cryo-stage setup provides for the first time 3-D-data on the individual inner pore shape delineation down to µm spatial (voxel) resolution of sub-mm small naturally as well as wind tunnel rimed graupel particles. Special care must be taken for maintaining a cooling chain between sampling and measurement. It must be kept at liquid nitrogen temperature (77 K) until measurement of the original structure at the µm spatial scale. However, even at that temperature there is no chance to preserve any ice bubble structure at sub-µm spatial resolution due to the Kelvin effect. In natural graupel grains, Y-shaped morphology of air-filled pores was found. This morphology transformed into smaller and rounded voids well-known from literature when the ice particle was annealed for as short as half an hour at 265 K and must, therefore, be regarded as artificial rather than representing the in situ pore structure. With the new synchrotron tomography approach, quantitative information on the in situ pore structure statistics within individual samples representative for a known or, thus, deduced growth mode or history can be derived, in particular if combined with airplane sampling in the troposphere at in situ growth conditions.

1 Introduction

The evolution of hydrometeors in the atmosphere is coupled to a variety of microphysical processes such as thermodynamics and radiative heating (Pruppacher and Klett, 1997). For multidimensional Eulerian and Lagrangian numerical weather prediction models, representation of ice microphysics in atmospheric clouds poses a challenge

AMTD
3, 4761–4789, 2010

due to accurately representing the evolution of discrete particles contained within. Recent approaches try to evolve properties of ice particles such as the dynamics of size distribution in such a way that the ambient conditions along a trajectory of ice particles are reflected in gross geometrical particle property variables (Hashino and Tripoli, 2008). They are integrated based on the respective microphysical processes that the ice particles are experiencing, in particular collision-coalescence processes and resulting habit changes. The shape and habit of ice particles is full of variety as evidenced by numerous optical microscope images (e.g., Libbrecht, 2005; Bailey and Hallett, 2009). Ice particles grow to precipitation sizes at the expense of liquid drops by diffusion of water vapour (Bergeron-Findeisen process) or by riming in convective clouds. The latter process yields in graupel grains which cannot be classified into simple geometrical categories such as snow crystals due to its rimed exterior formed by a supercooled droplet condensation process (Pruppacher and Klett, 1997; Von Blohn et al., 2009).

A typical feature of graupel grains is their opacity due to air bubbles formed during freezing of the riming droplets. Both the surface roughness and opacity of the hydrometeors have an impact on light scattering properties and, hence, the radiation properties in clouds. The effect of the air bubbles within ice crystals is to reduce the backscatter in comparison with the case of bubble-free ice crystals. These features vary with the number, sizes, locations, and shapes of the air bubbles within the ice crystals. Moreover, the asymmetry factors of inhomogeneous ice crystals decrease as the ratio of air-bubble volume to ice crystal volume increases. A study to examine the impact of accounting for air bubbles in ice crystal morphology on the retrieval of ice cloud optical thickness and effective particle size revealed recently that the reflectances simulated for inhomogeneous ice crystals are larger than those computed for homogeneous ice crystals at a wavelength of 650 nm (Xie et al., 2009). Thus, the retrieved cloud optical thickness is reduced by employing inhomogeneous ice cloud models. This effect implies, particularly in the case of large air bubbles, that the retrieved effective particle size for inhomogeneous ice crystals is larger than that retrieved for homogeneous

AMTD
3, 4761–4789, 2010

ice crystals. Therefore, the porosity of hydrometeors can eventually be considered to affect the Earth's climate.

The common bulk density of graupel between 0.05 and 0.9 g/cm^3 is dependent on the amount of the air bubbles that are included, which in turn depends on the dominant growth regime (Pruppacher and Klett, 1997). Measurements by optical microscope of the crystal size and porosity in thin sections by Carras and Macklin (1975) and others in the 70 s were used quantitatively to deduce the growth history of graupel and hailstones. This effort ultimately ceased in the mid 80s once it became clear that the internal structure is quite sensitive to annealing during sample handling. This renders any quantitative scheme for the determination of growth conditions doubtful (Ashworth et al., 1980; McCappin and Macklin, 1984). More recent information about the porosity structure in pristine atmospheric ice particles is generally scarce, despite its importance to environmental microphysics and chemistry. The use of 2-D microscope techniques is not always justified in having access to 3-D microphysical parameters, because the correlations are not always linear. Traditional 2-D imaging techniques, e.g., cannot constrain higher-order geometrical attributes which can cause, for example, an under-estimation of the specific surface area. The 3-D topography of a graupel particle has not yet been recorded with an optical microscope because of the limited depth of field in the instrument. X-ray absorption micro-tomography (XMT) overcomes this imaging problem by providing non-destructive, cross-sectional as well as 3-D object representations from X-ray attenuation mapping. This approach has primarily been developed in the last decade by research groups interested in simulating the time-lapse microstructure transformations of snow (the term "metamorphosis" is used instead of "annealing" in the related geosciences community which we tend to apply here as well). Schneebeli and Sokratov (2004) performed micro-tomography on fresh snow samples using a bench-top tomography device located in a 'walk-in' cold room and equipped with a conventional X-ray tube which allows for a spatial resolution of as low as 10 µm per voxel. Determination of the real specific surface area of fresh precipitates is, thereby, possible as recently verified by gas adsorption

AMTD
3, 4761–4789, 2010

experiments (Kerbrat et al., 2008). On the other hand, synchrotron radiation produces orders of magnitude more intensive and perfectly collimated X-ray beams. It is particularly adapted to the study of ice microstructure, because it gives similar µm-resolution images but in a much shorter scanning time (1–2 h; Coléou et al., 2001). To our knowledge, however, this is the first 3-D tomographic report of pores in natural sub-mm (≤1 µL) sized atmospheric ice particles at µm spatial resolution. Moreover, we demonstrate shape metamorphism processes at the inner air-ice interface of an individual graupel particle observed in situ in a time-lapsed experiment at 265 K, and demonstrate quantitatively which sample-handling temperatures are required to preserve the in situ ice particle structures.

2 Material and methods

2.1 Particle sampling and preparation

Artificial graupel grains were produced in the vertical wind tunnel of Mainz University developed to study the collision coalescence growth of single spherical ice particles while they were freely levitated in a laminar flow containing a cloud of supercooled droplets (Von Blohn et al., 2009). The frozen collector particles' radii were initially about 300 µm, and the collected supercooled droplets with a median volume radius of 15 µm. The experiment was performed in the dry growth regime at temperatures of $-10 \pm 2\,^{\circ}$C where riming commonly proceeds in the atmosphere. The graupel collected about 160 droplets per second which yield an increase of about 200 µm in volume radius during the 60 s duration of the experiment. Thus, one of the rimed ice particles was extracted from the wind tunnel column by a manually controlled suction box, sealed airtight in a plastic vial (Zinsser Analytics), and stored under dry ice ($-78\,^{\circ}$C) until analysis a couple of days later. Natural spring graupel samples were collected at the university campus on 30 March 2005. The weather was determined by a stable air mass boundary system with graupel showers due to a frontal wave at the day of

AMTD
3, 4761–4789, 2010

sampling. The temperature 2 m above ground was 9 °C. The precipitating graupel particles were collected in an open dewar vessel filled with liquid nitrogen. By this method the particles were quenched at −196 °C to preserve their original morphology. A black tissue besides the dewar was used to monitor if still graupel or already snow is precipitating into the vessel. Once graupel was changing into snowflakes, the dewar was sealed immediately and stored in a dry ice box until all liquid nitrogen evapourated. Any snowflakes were manually removed from the sampled particles in a cold room laboratory. Single graupel grains were sealed airtight in Zinsser vials and stored under dry ice until analysis a couple of days later. Another set of ice particles were collected at the Swiss High Alpine Research Observatory Jungfraujoch (Switzerland) during the Cloud and Aerosol Characterisation Experiment 5 (CLACE-5) campaign. The Sphinx research platform of the Jungfraujoch observatory (3580 m a.s.l., 46.55° N, 7.98° E) is situated on the northerly crest on a mountain saddle between the mountains Jungfrau (4158 m a.s.l.) in the west and Moench (4099 m a.s.l.) in the east within the glacier accumulation zone where monthly mean temperatures are below 0 °C all year around. Due to its high elevation, the observatory is mostly covered in cloud during snow fall periods (Baltensperger et al., 1991). Similar to the procedure described above, a dewar partly filled with liquid nitrogen was exposed to the precipitation at the station. Meteorological information during sampling was obtained from the automatic meteorological station of the Swiss Meteorological Institute located on the same platform. Air temperature was −15 °C at snowfall sampling time 10:10 UTC+1 on 7 March 2006. The transport of the collected ice particles was , thus, made in a well-isolated and electrically cooled box filled with dry ice. After arrival in our cold room laboratory, the snowflakes were removed manually and the remaining graupel grains subsequently stored in Zinsser vials under liquid nitrogen. For transport to the tomography beamline, the vials were sealed inside a plastic bag, which was further embedded in a dewar filled with tris-poly-ethyl-butyl-ether ($C_{13}H_{28}O_4$). The temperature of this organic solvent (210 K) was adjusted by manually adding liquid nitrogen to it (Feldmann et al., 1994). The samples arrived at the synchrotron beamline a couple of weeks after the

AMTD
3, 4761–4789, 2010

respective sampling campaign. The plastic containers were immediately removed from the transport unit and placed inside a cold box filled with fresh dry ice. The dry ice box was then extra cooled by placing it in liquid nitrogen until measurement.

2.2 Cryo-tomography setup at SLS beamline MS-TOMO

Micro-tomography was performed at the endstation "MS-TOMO" of the materials science beam line X04SA at the Swiss Light Source (SLS), which has been detailed elsewhere (Stampanoni et al., 2002). A monochromatic X-ray beam ($\Delta E/E = 0.014\%$ at 10 keV and 300 mA electron current of the synchrotron injected in top-up mode) was used when taking the tomograms. The beamsize was set to a final field-of-view of 1.4 mm^2 tailored by a slit system. The radiographic projection of the sample was taken from a Ce-doped YAG scintillator screen (Crismatec Saint Gobain, Nemours, France) and digitized by a high-resolution CCD-camera (Photonic Science Ltd., UK). As an extension of the standard setup, ice samples need to be cooled during measurement. The samples are stored and measured in a sample holder specifically developed for the ice particle analysis (Miedaner et al., 2007; Murshed et al., 2009). However, experiments with sub-mm ice particles are challenging and require a stringent control of temperature and water condensate formation as detailed in the following. The sample holder was custom-made of a polyamide cup that can be closed air-tight with a polyamide cap which bears a metal tip (Fig. 1). This tip aids in centering the specimen to the rotational axis. The polyamide walls surrounding the sample chamber were 2 mm thick each, and the bottom was drilled into a conical shape to simplify positioning of the ice particle on the rotational axis of the beamline goniometer. The ice particles were analysed with or without embedding in an organic cyclohexane matrix (melting point 260 K, therefore, solid at the measurement temperature). During the measurement the temperature was recorded using a PT-100 RTD element ($2 \times 2.3 \times 0.9$ mm; Greisinger Electronics, Germany). These measurements were not taken continuously but once per second for duration of less than 0.2 s in order to minimize the heating of the sample by the PT-100 element. The accuracy of the sensor was specified as $\pm 1\,^{\circ}C$. The

AMTD
3, 4761–4789, 2010

sample holder was placed into the standard goniometer mount at the beamline. Prior to measurement, all tools required for sample handling and mounting were kept inside an isolating box filled with dry ice for temperature preconditioning. For cooling a flow of cold nitrogen gas was provided from the nozzle of a Cryojet-XL (Oxford Instruments, UK), directed on top of the sample cup. A cage of two concentric Kapton tubes was taped airtight onto the standard cryojet nozzle (Fig. 1). These tubes were kept at a constant distance to each other by two aluminum rings located at the top and bottom of the cage. The cryojet provides two concentric gas flows enclosed by the inner Kapton foil and directed to the sample cup (Fig. 1). The cold gas outflow from the inner cryojet tube ($10\,\mathrm{L\,min^{-1}}$ at ca. 210 K and 8 mm in diameter) can be temperature controlled in steps of 0.1 K as specified. The outer one of dry shielding nitrogen flow ($2\,\mathrm{L\,min^{-1}}$) is designed to protect the cryojet nozzle from icing due to water condensation, and was kept at room temperature (10 mm in diameter, about 295 K). Fast and well-defined changes in temperature can be established by changing the mixing ratio of both flows. The total outflow of nitrogen of $12\,\mathrm{L\,min^{-1}}$ was strong enough to prevent any back circulation of ambient humid air from the beamline hutch into the cage, even when turbulent mixing occurs due to the presence and movements of the sample-holder. The region between the two concentric Kapton hoses was flushed additionally with dry nitrogen at room temperature from a gas cylinder (approx. $0.9\,\mathrm{L\,min^{-1}}$). As this N_2 flow escaped via two small holes at the bottom between the two foils, any back-diffusion of humid air into this region was prevented. Thus, no condensation of ambient humidity occurred on the inner cold or on the outer warm Kapton foil, which both served as a window for the X-ray beam. Such a condensate in the optical path during the experiments would have biased the sample tomograms significantly. The energy of the synchrotron beam was adjusted to 10 keV to increase the contrast as well as to reduce possible heating effects in a run without the organic embedding. Beam intensity fluctuations are minimized at SLS due to the top-up injection mode (300 ± 1 mA) and special beamline setup (Stampanoni et al., 2002). However, in order to correct any beam instabilities and to ensure high quality, darks and flats were taken every 50 angular steps. During this procedure,

AMTD
3, 4761–4789, 2010

the sample holder was moved out of the X-ray beam towards the inner wall of the surrounding cage, where the temperature is slightly higher than in the centre. This is a very critical moment, because temperature gradients may cause shape metamorphism of the internal ice microstructure (Colbeck, 1983). To minimize possible temperature fluctuations, the outer (warm) gas flow was stopped 2 s before moving the sample. It was switched on again 2 s after the sample had been returned to the centre. This procedure limited temperature changes in the sample holder to less than 3 degrees, as recorded by the RTD element. However, this temperature sensor was mounted at the bottom of the sample holder with a much better thermal contact to the surrounding gas compared to the ice sample. Moreover, the sensor is embedded in a glue of lower isolating capacity than the sample holder itself. The high heat capacity of the relatively thick polyamide walls additionally helped to stabilize the sample thermally. This is corroborated by heating rate estimates of the upper limits for temperature changes of the sample holder. Therefore, a fully prepared polyamide cup was frozen at 240 K and then suddenly exposed to room temperature. As 263 K were never reached in less than 40 s during those runs, which yield a maximum heating rate of less than 0.8 K s^{-1}. Therefore, the maximum temperature change, as recorded by the RTD element at the bottom of the sample holder, could not exceed 3 degrees during the 6 s required for a full darks and flats imaging run. Hence, the measured temperature fluctuation poses an upper limit to temperature variations during the experiment. Unfortunately, cold gas leaving the Kapton cage could not be prevented flowing towards the goniometer stage and scintillator screen. To avoid water condensation from the ambient humidity, an additional fan tubing was mounted on the sample support to suck the cold gas stream away from the goniometer stage and, hence, also further reduce any possibility of water condensation via cold bridge effects. To our own experience, the latter effect could easily damage sensitive detector electronics.

AMTD
3, 4761–4789, 2010

2.3 Data processing

For a three-dimensional micro-tomography of one particle, 1000 individual X-ray transmission images of the sample are taken while rotating it over 180° relative to the fixed beam. These slice projections are used to reconstruct the three-dimensional image of the investigated object using an appropriate reconstruction algorithm (Herman, 1980). The tenfold magnification of the microscope provides a maximum field-of-view of about 1.4 mm × 1 mm at a spatial resolution of 0.7 µm. However, to increase the signal-to-noise ratio, the recorded data were immediately hardware-binned resulting in a final 1.4 µm edge length per voxel. An exposure time of two seconds per slice yields in roughly one hour of measuring time including mounting and sample preparation. The 16-node Linux cluster computer facility at the SLS allowed for the generation of sinograms from the XMT data on-the-fly because reconstruction into horizontal slices could be performed within a few minutes. Therefore, a first evaluation of the image quality could be ventured immediately after the scan finished using the VSG Amira/Avizo software package. It is critical to accurately preserve the boundaries between pores and ice because mislabelling on the boundary voxels could lead to over- or underestimating the pore space. The very low absorption contrast between ice and air (or the embedding cycloheptane matrix) hampers automatic gradient thresholding for segmentation. Noise was first smoothed out without smoothing the high gradient areas, i.e., fast transitions between low and high densities like in a colour diffusion process (Herman, 1980). Smear-out effects known for Gaussian type filters used in curvature-driven grain segmentation algorithms (e.g., Brzoska et al., 2007) were also avoided. Instead, an edge sensitivity algorithm was implemented using Matlab that stops the edge-preserving smoothing filter at a voxel where an edge is detected. Amira/Avizo provides conveniently for a Matlab (and C++) bridge for this and other custom extensions. As the camera was in a distance of approximately 3 cm from the object, refraction enhances the ice/air interface, which in turn allows a clear identification of the ice/air boundaries even by visual inspection. In the final slices, the component with the lowest X-ray

AMTD
3, 4761–4789, 2010

absorption was coloured white (maximum CT-number of 255) while the strongest absorption appeared black (minimum CT-number of 0). The optimum threshold between ice and air was determined by fitting a sum of two Gaussian curves to the grey scale histograms (CT numbers) and calculating the intersection of the individual Gaussians (Sonka et al., 1999). This procedure effectively minimizes the number of spurious voxels introduced in the segmentation process. The optimum threshold was determined for each tomogram, and the mean for each class was finally applied to segment the images. Variations around the mean optimum threshold for all measurements of a particular class leads to an uncertainty in threshold, and finally leads to an uncertainty in average surface and volume estimation as discussed below.

2.4 Volume and surface estimation

All segmented pores were assigned to an individual object, for each of which the volume and surface area could be determined. Unfortunately, the AMIRA software codes the output of this algorithm in a byte structure which allows a maximum of 255 objects per ROI, although the whole sample (1023 slices) contains much more than this. Therefore, the entire dataset was cut into image stacks of 50–100 slices to obtain less than the maximum permissible number of pores per stack. A drawback of this relief is that the data suffer now from an artificial surface area increase at the cutting planes. To reduce the weight of these errors, the total surface area in the whole picture was determined by assigning all segmented voxels (same threshold values) to one single object. The latter data were used to calculate the average surface area of the representative individual pore as well as its average volume. The volume-to-surface ratio was determined for each pore individually as discussed below. In this case, the artificially created surface area due to the cutting did not cause an error greater than 15% due to the predominance of "uncut" pores in the whole dataset statistics. For the next data preprocessing step, a triangulation procedure is necessary for reliably determining the effective properties such as the specific surface of the inner porosity. Triangulation is the art of creating a complex surface from a cloud of points in 3-D space by setting

AMTD
3, 4761–4789, 2010

up reliably fitting polygons. Various criteria have been developed to evaluate to what extend the triangulated surface represents the real shape of the objects (e.g., Brzoska et al., 2001). We used a Delaunay algorithm implemented within the AMIRA code to build a finite-element representation of the objects. The sensitivity of our setup with respect to the total pore volume present in the sample was estimated by averaging in subsequently growing volumes. The dataset was artificially binned to a 2, 4, 6, 8, and 10 times the resolution using the routines provided by a Lanczos filter (Herman, 1980). Then the voids were segmented using the same threshold values as discussed above. The total volume determined was plotted versus the edge length of the voxels (1.4, 2.8, 4.2, and so on up to 14 µm). The increase in the detected volume vanished for the smallest three voxel lengths (1.4 to 4.2 µm). Assuming that these changes in volume can be extrapolated to a fictive voxel length of 10 nm (i.e., >0), we found that approximately 97% of the extrapolated total volume was detected at a spatial resolution of 1.4 µm. The further data analysis involved quantification of the number, individual volumes, and surface areas of voids based on the "burning algorithm", frequently used in percolation models to assess the connectivity of a phase in a microstructure (Stauffer and Aharony, 1994). The burning algorithm is a way of identifying all members of a cluster of connected voxels that span the image. The common procedure is to start on one side of an image, "burn" one pore voxel by setting its gray scale to another number that is not in the existing range, e.g., not in the range 0–255, and set any pore voxel that touches this voxel to the same number. Then continue this process until there are no more "unburned" pore voxels left that are touching the last burned voxels. The process is similar to classifying all voxels of a certain gray value as being combustible, and then touching a match to one of them. If the "fire" burns from one side of the image to the opposite side, then the burned voxels are said to form a spanning cluster, or percolate. This process can be repeated by starting the fire at any unburned voxel in order to identify all connected clusters, and all non-spanning clusters as well. This is an efficient way to determine if the pore space percolates through the digital image. It is important to note, however, that percolation thresholds are usually larger in 2-D than

AMTD
3, 4761–4789, 2010

in 3-D, i.e., the connectivity in 3-D and 2-D is fundamentally different. A graupel grain is generally regarded as a porous spheroid moving in the orientation which offers the maximum drag to motion. Its cumulative pore volume distribution (in percentages) is determined based on the following equation:

$$V_C(k) = \sum_{k=0}^{k} \frac{V_k}{\sum_{i=0}^{N} V_i} \cdot 100 \quad (1)$$

where the index i sorts N pores by size, with the small pores at low i, and V_i represents the pore volume per particle in μm^3. The volume-to-surface ratio was also determined for each individual pore as commonly used to characterise porous materials (Brunauer et al., 1967). The porosity is reported as the ratio of the number of void voxels to the total number of voxels in the total volume of the sample. The average volume and surface area were calculated as the total volume to surface area divided by the number of identified pores. Thus, the obtained geometrical characteristics are summarized for all samples in Table 1.

3 Results

3.1 Ice particles from the Mainz wind tunnel

The ice particle collected during the riming experiment in the vertical wind tunnel of the University Mainz (Von Blohn et al., 2009) showed a quite inhomogeneous distribution of the air bubbles. The collision with cloud droplets increased the particle radius by 1.4 times, hence, doubling the particle surface area from $2.5 \times 10^6 \mu m^2$ to $5.1 \times 10^6 \mu m^2$, and tripling the particle volume-to-surface ratio from 10 µm to 27 µm. The artificial graupel grain contained air bubbles only in the original frozen ice core (Fig. 2). Surprisingly, upon riming no additional air bubbles larger than the obtained spatial resolution of 1.4 µm were found. Possible reasons for this have been discussed already in a previous paper (Von Blohn et al., 2009).

AMTD
3, 4761–4789, 2010

3.2 Ice particles from Swiss high alpine observatory Jungfraujoch

Five individual particles collected during the CLACE-5 campaign were finally analysed at the tomography beamline. In two opaque samples air bubbles were found distributed more or less homogeneously over the whole sample (Fig. 3). The porosity of only 0.5% of the first particle CLACE #1 is representative for high density rime. Bubbles found in this sample were of an average volume of 9.3×10^{-9} mL, and an average surface area of 3.0×10^{-9} m^2. The volume-to-surface ratio reached a value of 1.0 µm, while the inner-to-outer-surface ratio was 0.11%. CLACE particle #2 showed a slightly different feature. It was more densely aggregated compared to the rather fragile CLACE particle #1. Like in the previous sample, the air bubbles were homogeneously distributed and posed an average volume of 4.7×10^{-9} mL and an average surface area of 2.6×10^{-9} m^2. Solid or biological particles like black carbon or lichen, known to act as ice nuclei (e.g., Cozic et al., 2008; Henderson-Begg et al., 2009), could not be detected at the spatial resolution of 1.4 µm. The three other particles were of clear ice, had no dendritic habit and showed no inclusions of solid or liquid impurities, neither of air bubbles. The degree of possible riming could ultimately not be determined in the particles due to limited contrast between individual adjacent ice crystals.

3.3 Graupel pore structure

Air filled pores in the two mm-sized graupel grains collected at Mainz university campus were Y-shaped with a high connectivity (Fig. 4). The average volume occupied by air in the graupel grain #1 was 3.6×10^{-10} mL, with an average surface area of 4.9×10^{-10} m^2. Interestingly, one part of the grain was just pure ice without any inclusions. The second graupel grain (graupel #2), embedded in freshly molten cycloheptane for mechanical stabilization during the measurements, exhibited spherical pores with an average volume of 3.7×10^{-10} mL and an average surface of 3.9×10^{-10} m^2. These values are similar to those obtained for CLACE particle #1, as detailed above, irrespective of the different sampling conditions, and may be a common shape variation

AMTD
3, 4761–4789, 2010

for graupel. However, based on our dataset and the limited amount of samples which do not provide any statistical information on their representativeness, different conditions of formation (e.g., higher temperatures or longer atmospheric residence times in reservoirs of warmer air before sampling) cannot be ruled out. No further inclusions apart from air were found inside the grains. If at all present, they may have been of such a low concentration that no significant absorption contrast could be reached. Again no trace of a kernel or of impurities apart from air could be detected inside the particles at the spatial resolution.

3.4 Graupel metamorphism

Ice grain metamorphosis (recrystallization due to annealing) induced by temperature cycling of the graupel sample was elucidated by performing first analysis at 230 K (graupel grain #1), another one after increasing the temperature to 265 K and half hour equilibration (graupel grain #1c). This latter temperature is in the range between −8 and −12 °C, where riming proceeds in the atmosphere, but well below 0 °C as used in previous annealing tests (Knight et al., 1978; Ashworth et al., 1980; McCappin and Macklin, 1984). Thus, the induced isothermal metamorphosis drastically changed the microstructure from graupel #1 into #1c. The originally Y-shaped pores became disconnected and more spherical which minimized the free energy of their surfaces (Fig. 4). There are two likely mechanisms for this isothermal annealing, (i) surface diffusion, or (ii) vapour transport and redeposition within the pores, driven by the Kelvin effect. Nonetheless, the average pore surface area only slightly decreased from initially 4.9×10^{-7} m^2 to 4.1×10^{-7} m^2 during the experiment, and also the average pore volume kept approximately constant (3.6×10^{-10} mL before metamorphism and 3.5×10^{-10} mL in the metamorphosed state; Table 1). However, both the absolute number of pores found in the graupel grain and the overall porosity decreased during annealing (Table 1) indicating some loss of air during annealing.

AMTD
3, 4761–4789, 2010

4 Discussion

4.1 Sample stability

As stressed already by Knight et al. (1978), the importance of rapid recrystallization of ice particles can hardly be overestimated. Such early metamorphism is accompanied by a loss of information, and, if not recognized, can cause false conclusions being reached. The rate of isothermal recrystallization of ice particles strongly decreases with temperature (Colbeck, 1983; Cabanes et al., 2003; Flin et al., 2003; Domine et al., 2003; Legagneux et al., 2003). During the extended time of storage in dry ice, or during the transport of the CLACE samples from the Swiss High Alpine Observatory to our Mainz laboratory and back to the Swiss SLS synchrotron facility, shape metamorphism could have well occurred to the ice particles. However, the following arguments suggest that the geometrical characteristics of the samples did not change significantly. First, we were able to measure Y-shaped air bubbles, while the air-filled voids of aged ice particles are usually spherical due to the Kelvin diffusion effect as demonstrated by our isothermal metamorphosis experiment. If our samples would have experienced a significant degree of metamorphism, we should not have measured any changes in shape of the trapped voids as we enforced early metamorphosis at higher temperatures.

Thermodynamically, ice metamorphism is driven by the minimization of the overall surface energy of the ice particle, which leads to a smoothing of the ice surface (Colbeck, 1983). During this smoothing, the ice can be transported by two mechanisms, either by surface diffusion or by transport through the gas phase. The latter mechanism is driven by the Kelvin effect, which enhances the vapour pressure above convex surfaces compared to flat interfaces. The time scales for smoothing a half-sphere residing on a flat surface can, thus, be determined using the approach described recently by Kerbrat et al. (2008). They suggested a simple parameterization to assess the characteristic time scales for both mechanisms and, hence, can be used to calculate the characteristic time scale for the metamorphism process. To calculate the characteristic time t_D for surface diffusion, we use the equation $t_D = R^3/dD_s$, with the radius R of the

AMTD
3, 4761–4789, 2010

half-sphere, the diffusion constant D_s of water in a surface (quasi-liquid) layer on the ice surface and the thickness d of the surface layer. The latter is assumed at $d = 100$ nm at $-1\,^{\circ}$C, with a temperature dependence $d \sim ln(1/T_0 - T)$ below the water freezing temperature $T_0 = 0.00\,^{\circ}$C or 273.16 K (Dash et al., 1995). The characteristic time t_K for metamorphism by vapour transport is calculated by $t_K = \gamma\, R^2/(3\,\exp(C/R\text{-}1))$, where $C = (2\, m_{H_2O}\sigma)/(k_B T \rho_{ice})$ and $\gamma = r_{ice} k_B T/(m_{H_2O} Dp_{flat})$, with the radius of asperity, R, the mass of the water molecule, m_{H_2O}, the surface energy of ice, σ, the Boltzmann constant, k_B and the density of ice, ρ_{ice}.

In Fig. 5, we show a calculation of the characteristic times for different temperatures. Even at temperatures as low as 265 K the smoothing of the surface due to the Kelvin effect is very fast, and structures of the size of several micrometers can disappear during typical times of tomographic measurement, let alone any extended storage at that temperature. On the other hand, if we calculate the size of the pore asperities which would still be present in a sample stored one week under dry ice at 200 K, we find that all asperities having a radius lower than 2 µm may have disappeared. This radius corresponds to the actual resolution of our synchrotron tomographic approach. The calculation also suggests that during the scan of a sample of about one hour made at 230 K, asperities with a diameter of less than 2 µm present at the beginning of the scan will disappear during the measurement. Therefore, we conclude that any sample metamorphosis which occurred during collection, subsequent storage, and transport in LN_2 could hardly be detected at the available spatial resolution. According to the results of this calculation it is virtually impossible to measure in situ ice structures with tomography at sub-µm spatial resolution upon any affordable sample handling conditions.

4.2 Graupel structure

Riming droplets do not freeze right away when they are deposited on the ice surface, but the accreted water changes phase depending on the heat transport from the graupel into the environment (so called “wet growth regime”). While the formation

AMTD
3, 4761–4789, 2010

of spherical and round bubbles was discussed theoretically and on experimental basis already three decades ago (List, 1958; Knight and Knight, 1968; List et al., 1972; Macklin et al., 1976), little is known about the formation of non-spherical bubbles which must have a higher interface free energy than spheroid bubbles. Their Y-shaped morphology is probably related to the void wedges at the triple junctions between fast frozen droplets retaining approximately their spheroid shape, and do not occur in a preferred orientation. This feature is unlikely for the wet growth regime because the contact angle between water and ice is relatively low, which would, therefore, lead to a relatively rapid fluid migration along the grain boundaries.

Since air is soluble in water but insoluble in ice, air is rejected at the ice-water interface upon freezing. If the freezing proceeds rapidly, freshly formed tiny air bubbles are trapped by the advancing ice interface, producing a milky or opaque ice. If the freezing proceeds slowly, the air has a chance to coagulate into larger bubbles and eventually escape to the surrounding atmosphere promoted by supercooled fluid drainage along the connected pore network (Pruppacher and Klett, 1978). This could well explain the apparently bubble-free rim of the artificial graupel grown in the wind tunnel of Mainz University at a relatively slow rate of 3.7×10^{-4} cm s^{-1}. For the natural graupel grains, we calculated the volume of entrapped air for the measured bubbles and compared this with the corresponding volume of dissolved air in the same volume of supercooled droplets at $-10\,^{\circ}$C (Table 1). This ratio is below unity for the graupel particle #2 which includes more spherical air bubbles of greater mean void size (Table 1). If to compare with the respective nomograms of this ratio vs. freezing rate derived by laboratory experiments (Carras and Macklin, 1975), then these graupel particles would fit to relatively slow freezing rates of the order 1×10^{-3}–5×10^{-3} cm s^{-1}. However, this ratio is well above unity for the three other ice particles studied (Table 1). This behaviour can be understood if we consider not only diffusion of the air bubbles originally entrapped within the freezing droplets towards the grain boundary intersections, but also additional air entrapped between individual cloud droplets upon instantaneous freezing as indicated by the Y-shaped voids. Clearly, not much diffusion of air enclosed by the

AMTD
3, 4761–4789, 2010

droplets while freezing could have happened which indicates relatively rapid freezing rates. The latter is typical for low density rime ice, even though it is not the case here. This may suggest that the graupel grew with a density less than 0.3 g cm^{-3} under an early dry growth regime at lower T_d's, but became somewhat soaked at later (minutes?) wet growth stages at higher T_d's. Such a natural growth history bias is not readily compatible with the simple bubble size and number criterion for graupel growth given by Carras and Macklin (1975) or Macklin et al. (1976). In spite of this negative result, research will continue on this highly interesting question. For if it were to prove correct, then the consequences would be enormous to say the least.

5 Summary and conclusions

Air bubble size distributions, concentrations and structures are important clues in identifying the growth regime of graupel and hailstone. This study yields in the first report of tomographic 3-D analysis of micrometer-sized air voids in mm-sized ice particles such as in this case freshly precipitated graupel grains. A resolution of 700 nm (without binning) was achieved within less than one hour acquisition time, already at the time the setup was first tested for this study. However, because technology is rapidly advancing the scanning time is presently (end of 2010) already reduced to minutes. This relatively rapid measurement time is warranted in preserving the in situ inner structural features of graupel grains as quantified in this study. The most important prerequisite is namely to avoid any recrystallization during sample handling. Special care must be used to collect fresh graupel (and hail) by quenching it preferably in liquid nitrogen; but even with such good collection techniques care must be taken to estimate the possible degree of recrystallization. This care includes a stringent control of the cooling chain at LN_2 temperature between sampling (preferably airplane sampling in the troposphere at in situ growth conditions) and measurements to qualify any deductions appropriately. The synchrotron-based micro-tomography then offers a just affordable but flexible base to perform process studies, such as changes in porosity entrapped by various growth

AMTD
3, 4761–4789, 2010

modes in ice. The timescale of the imaging process, therefore, allows, for example, studying isothermal metamorphism processes on atmospheric samples as demonstrated for a graupel grain. This early metamorphism was quantified by changes in shape delineation such as total volume and surface area of the voids. Clearly, our database is rather small yet unique. It should be understood that the technique presented here cannot be used to acquire statistical results on a number of particles but rather information on pore structure statistics within an individual sample representative for a known growth mode or history. With combined efforts of such advanced imaging technology revealing pore substructure largely unreported before, together with appropriate advancement in microphysical theory models, it would appear that our level of understanding regarding graupel and hailstone formation and effects is now poised for progress, in particular if combined with airplane sampling at in situ growth conditions.

Acknowledgements. This study was supported by DFG grant SFB 641 "The tropospheric ice phase" and the Excellence Cluster "Geocycles" of the German Federal State of Rheinland-Pfalz. Part of this work has also been supported by the European Commission under the 6th Framework Program through the Key Action "Strengthening the European Research Area, Research Infrastructures RII-CT-2004-506008" and by the EU Integrated Project SCOUT-O3. PSI-SLS beamline technicians M. Birrer, M. Lange, and D. Meister made this challenging experiment a success. M. Kerbrat provided us with his software code for the calculation of Fig. 5.

References

Ashworth, E. T., Ashworth, T., and Knight, C. A.: Cylindrical ice accretions as simulations of hail growth: III. Analysis techniques and application to trajectory determination, J. Atmos. Sci., 37, 846–854, 1980.

Bailey, M. P. and Hallett, J.: A comprehensive habit diagram for atmospheric ice crystals: confirmation from the laboratory, AIRS II, and other field studies, J. Atmos. Sci., 66, 2888–2899, 2009.

Baltensperger, U., Gaggeler, H. W., Jost, D. T., Nieveler, U. E., and Schwikowski, M.: In-cloud scavenging by snow at a high-alpine site, J. Aerosol Sci., 22, S541–S544, 1991.

AMTD
3, 4761–4789, 2010

Brunauer, S., Mikhail, R., and E. Bodor, E.: Pore structure analysis without a pore shape model, J. Colloid Interface Sci., 24, 451–463, 1967.
Brzoska, J.-B., Flin, F., Lesaffre, B., Coléou, C., Lamboley, P., Delesse, J.-F., Le Saëc, B., and Vignoles, G.: Computation of the surface area of natural snow 3-D images from X-ray tomography: two approaches, Image Anal. Stereol., 20(Suppl. 1), 306–312, 2001.
Brzoska, J.-B., Flin, F., and Ogawa, N.: Using Gaussian curvature for the 3-D segmentation of snow grains from microtomographic data, in: Physics and Chemistry of Ice, edited by: Kuhs, W. F., RSC Publ., Cambridge, UK, 125–132, 2007.
Cabanes, A., Legagneux, L., and Dominé, F.: Rate of evolution of the specific surface area of surface snow layers, Environ. Sci. Tech., 37, 661–666, 2003.
Carras, J. N. and Macklin, W. C.: Air bubbles in accreted ice, Quart. J. R. Met. Soc., 101, 127–146, 1975.
Colbeck, S.: Theory of metamorphism of dry snow, J. Geophys. Res., C88, 5475–5482, 1983.
Coléou, C., Lesaffre, B., Brzoska, J.-B., Ludwig, W., and Boller, E.: Three-dimensional snow images by X-ray microtomography, Ann. Glaciol., 32, 75–81, 2001.
Cozic, J., Mertes, S., Verheggen, B., Cziczo, D. J., Gallavardin, S. J., Walter, S. Baltensperger, U., and Weingartner, E.: Field observations of black carbon enrichment in atmospheric ice particle residuals suggesting a potential ice nucleating capability, J. Geophys. Res., 113, D15209, doi:10.1029/2007JD009266, 2008.
Dash, J. G., Fu, H., and Wettlaufer, J. S.: The premelting of ice and its environmental consequences, Rep. Prog. Phys., 58, 115–167, 1995.
Dominé, F., Lauzier, T., Cabanes, A., Legagneux, L., Kuhs, W. F., Techmer, K., and Heinrichs, T.: Snow metamorphism as revealed by scanning electron microscopy, Microsc. Res. Tech., 62, 33–48, 2003.
Feldmann, J., Graemping, R., and Hirner, A.: Determination of volatile metal and metalloid compounds in gases from domestic waste deposits with GC/ICP-MS, Fresenius J. Anal. Chem., 350, 228–234, 1994.
Flin, F., Brzoska, J., Lesaffre, B., and Pieritz, R.: Full three dimensional modelling of curvature dependent snow metamorphism: First results and comparison with experimental tomographic data, J. Phys. D. Appl. Phys., 36, A49–A54, 2003.
Hashino, T. and Tripoli, G. J.: The Spectral Ice Habit Prediction System (SHIPS). Part II: Simulation of nucleation and depositional growth of polycrystals, J. Atmos. Sci., 65, 3071–3094, 2008.

AMTD
3, 4761–4789, 2010

Henderson-Begg, S. K., Hill, T., Thyrhaug, R., Khan, M., and Moffett, B. F.: Terrestrial and airborne non-bacterial ice nuclei, Atmos. Sci. Lett., 10, 215–219, 2009.
Herman, G.: Image Reconstruction from Projections, Academic Press, New York, 1980.
Kerbrat, M., Pinzer, B., Huthwelker, T., Gäggeler, H. W., Ammann, M., and Schneebeli, M.: Measuring the specific surface area of snow with X-ray tomography and gas adsorption: comparison and implications for surface smoothness, Atmos. Chem. Phys., 8, 1261–1275, doi:10.5194/acp-8-1261-2008, 2008.
Knight, C. A. and Knight, N.: Spongy hail stone growth criteria I. Orientation fabrics, J. Atmos. Sci., 25, 445–453, 1968.
Knight, C. A., Ashworth, T., and Knight, N.: Cylindrical ice accretions as simulations of hail growth: II. The structure of fresh and annealed accretions, J. Atmos. Sci., 35, 1997–2009, 1978.
Legagneux, L., Lauzier, T., Dominé, F., Kuhs, W. F., Heinrichs, T., and Techner, K.: Rate of decay of specific surface area of snow during isothermal experiments and morphological changes studied by scanning electron microscopy, Can. J. Phys., 81, 459–468, 2003.
Libbrecht, K. G.: The physics of snow crystals, Rep. Prog. Phys., 68, 855–895, 2005.
List, R.: Kennzeichen atmosphärischer Eispartikel. 1. Teil: Graupel als Wachstumszentren von Hagelkörnern, Z. Angew. Math. Phys., 9, 180–216, 1958.
List, R., Murray, W. A., and Dyck, C.: Air bubbles in hailstones, J. Atmos. Sci., 29, 916–920, 1972.
McCappin, C. J. and Macklin, W. C.: The crystalline structure of ice formed by droplet accretion, II: Annealed samples and application, J. Atmos. Sci., 31, 2447–2455, 1984.
Macklin, W. C., Carras, J. N., and Rye, P.: The interpretation of the crystalline and air bubble structure of hailstones, Quart. J. Roy. Meteor. Soc., 102, 25–44, 1976.
Miedaner, M. M., Huthwelker, T., Enzmann, F., Kersten, M., Stampanoni, M., and Ammann, M.: X-ray tomographic characterization of impurities in polycrystalline ice, in: Physics and Chemistry of Ice, edited by: Kuhs, W. F., RSC Publ., Cambridge, UK, 399–407, 2007.
Murshed, M. M., Klapp, S. A., Enzmann, F., Szeder, T., Huthwelker, T., Stampanoni, M., Marone, F., Hintermüller, C., Bohrmann, G., Kuhs, W. F., and Kersten, M.: Natural gas hydrate investigations by synchrotron radiation X-ray cryo-tomographic microscopy (SRXCTM), Geophys. Res. Lett., 35, L23612, doi:10.1029/2008GL035460, 2008.
Pruppacher, H. R. and Klett, J. D.: Microphysics of Clouds and Precipitation, 2nd ed, Kluwer Academic, Dordrecht, The Netherlands, 1997.

AMTD
3, 4761–4789, 2010

Schneebeli, M. and Sokratov, A.: Tomography of temperature gradient metamorphism of snow and associated changes in heat conductivity, Hydrolog. Process., 18, 3655–3665, 2004.
Sonka, M., Hlavac, V., and Boyle, R.: Image Processing: analysis and Machine Vision, 2nd Edn., Thomson-Engineering, London, UK, 1999.
Stampanoni, M., Borchert, G., Wyss, P., Abela, R., Patterson, B., Hunt, S., Vermeulen, D., and Rueeggsegger, P.: High resolution x-ray detector for synchrotron-based micro tomography, Nucl. Instr. Meth. Phys. Res., A491, 291–301, 2002.
Stauffer, D. and Aharony, A.: Introduction to Percolation Theory, 2nd Edn., Taylor & Francis, London, UK, 1994.
Von Blohn, N., Diehl, K., Mitra, S. K., and Borrmann, S.: Riming of graupel: Wind tunnel investigations of collection kernels and growth regime, J. Atmos. Sci., 66, 2359–2367, 2009.
Xie, Y., Yang, P., Kattawar, G. W., Minnis, P., and Hu, Y. X.: Effect of the inhomogeneity of ice crystals on retrieving ice cloud optical thickness and effective particle size, J. Geophys. Res., 114, D11203, 12 pp., 2009.

AMTD
3, 4761–4789, 2010

Table 1. Geometric data obtained for the ice particles.

Particle	CLACE #1	CLACE #2	Graupel #1	Graupel #1c	Graupel #2
Surface (10^{-6} m^2)	2.0	2.9	1.5	0.37	7.4
Volume (10^{-4} cm^3)	1.52	1.65	2.65	2.66	3.38
Porosity (%)	0.46	0.49	0.13	0.08	0.02
Pores					
Total surface (10^{-7} m^2)	2.3	4.5	4.8	2.8	0.59
Average surface (10^{-10} m^2)	30	29	4.9 ± 3.3	4.1 ± 2.3	4.0 ± 3.2
Total volume (10^{-7} cm^3)	6.9	8.0	3.54	2.36	0.56
Average volume (10^{-10} cm^3)	93	47	3.6 ± 2.9	3.5 ± 2.2	3.7 ± 3.0
Number of pores (absolute)	75	170	987	680	151
Specific number of pores (cm^{-3})	4.9×10^5	1.0×10^6	3.7×10^6	2.5×10^6	4.5×10^6
Volume-to-surface ratio (µm)	1.05 ± 0.36	1.33 ± 0.70	0.95 ± 0.3	1.18 ± 0.38	1.32 ± 0.29
Inner-to-Outer Surface	0.11	0.15	0.32	0.75	0.01
Volume of air in pores/ volume of air in solution*	13	14	3.8	2.5	0.47

* Volume solubility at $T = -10\,^{\circ}$C and $p = 1$ atm (data from Carras and Macklin, 1975).

AMTD
3, 4761–4789, 2010

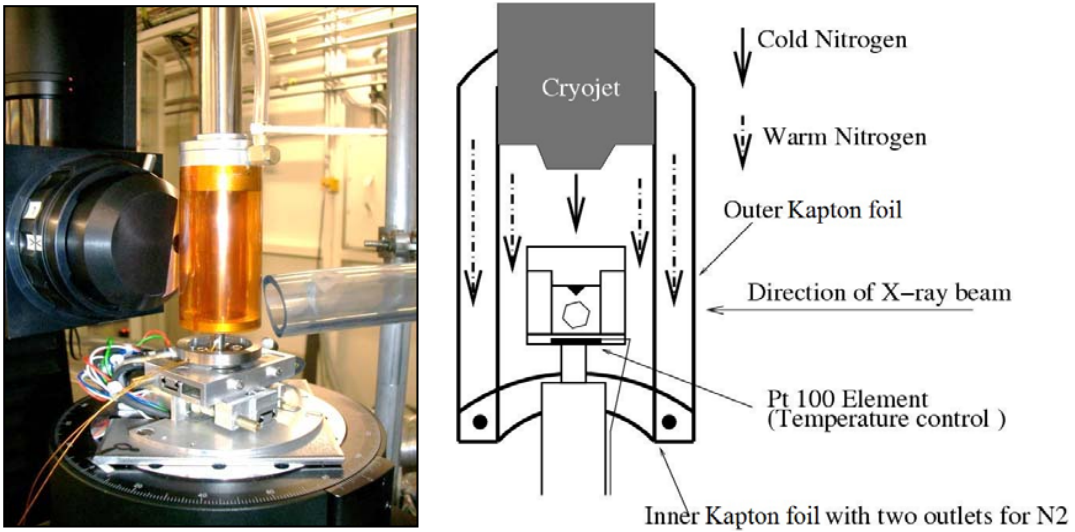

Fig. 1. Experimental setup with the XTM camera microscope on left side. A scheme of the invisible sample holder mounted within the double walled orange Kapton cage mounted on the cryojet nozzle is given on the right side. The Kapton cage can be slid up and down to facilitate sample exchange. The tube from the right pumps away the cold nitrogen exiting at the bottom of the sample holder to prevent water condensation on the goniometer stage.

AMTD
3, 4761–4789, 2010

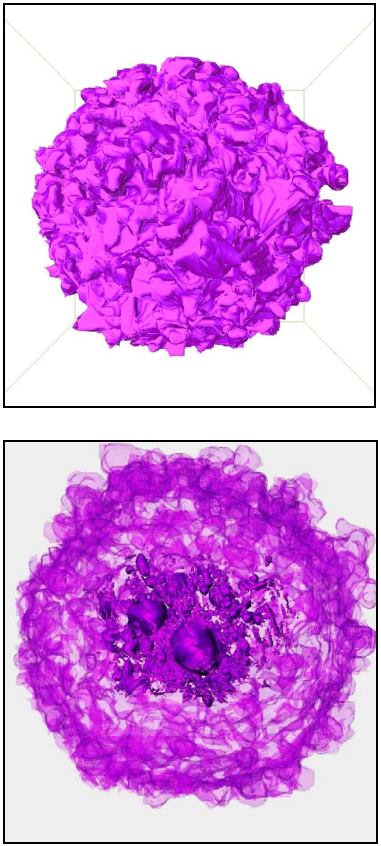

Fig. 2. Artificial graupel grain of 350 µm volume radius after 60 s of riming in the wind tunnel of Mainz University, with the outer surface (above) and the interior microstructure (below). The latter revealed air bubbles trapped only in the initial kernel droplet (darker features), while the rimed ice exterior (lighter features) appears bubble-free.

AMTD
3, 4761–4789, 2010

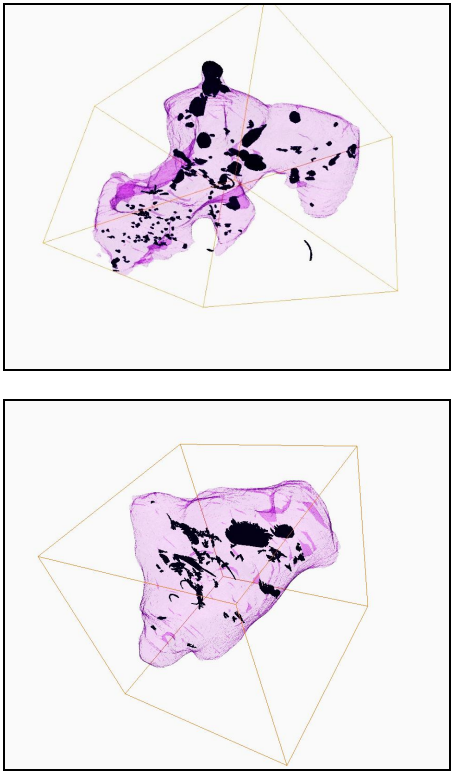

Fig. 3. Two particles collected at the High alpine Research Observatory Jungfraujoch (Switzerland) during the CLACE-5 experiment. The air-filled voids appear as black. The total edge length of the box surrounding the ice particles is $1 \times 1 \times 1$ mm. Note the different shape and size of the pores.

AMTD
3, 4761–4789, 2010

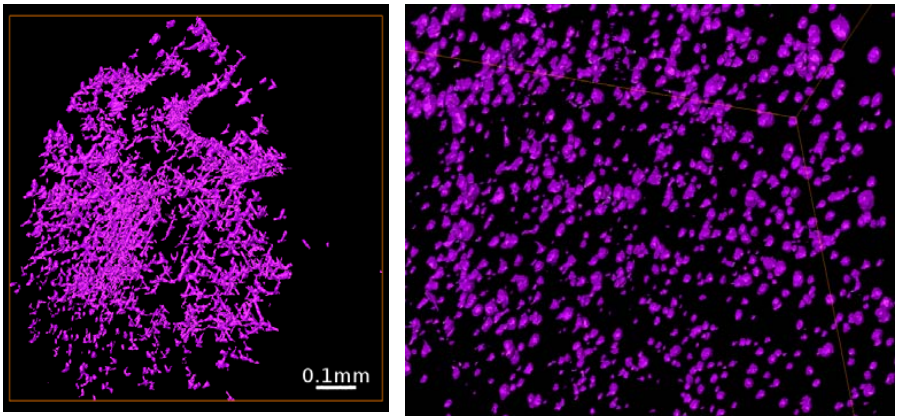

Fig. 4. Interior air filled bubble structures of a graupel grain (frames width 0.7 mm) showing the changes of the structures due to forced metamorphism, i.e. Y-shaped bubbles in the graupel grain sample #1 before (left), and spherical bubbles after 0.5 h annealing at 265 K in the graupel grain sample #1c (right).

AMTD
3, 4761–4789, 2010

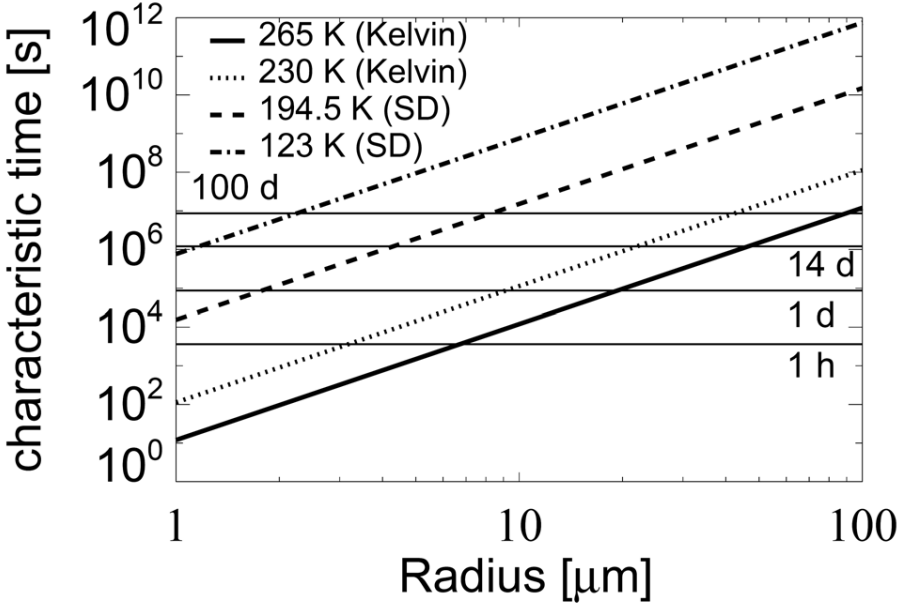

Fig. 5. Characteristic time for the smoothing of the ice surface due to surface diffusion (SD) or vapour transport (Kelvin) as a function of the initial radius of the pore asperity at two different temperatures representing sample handling conditions.

AMTD
3, 4761–4789, 2010